AUT Journal of Mechanical Engineering

AUT J. Mech. Eng., 6(3) (2022) 443-466
DOI: 10.22060/ajme.2022.20549.6005

Triply Periodic Minimal Surfaces Scaffolds and Their Comparison with Cancellous Bone: Fluid Flow Point of View

A. Parandvash, M. Rezaei, E. Khavasi*

Department of Mechanical Engineering, University of Zanjan, Zanjan, Iran

ABSTRACT: The present study investigated bone growth characteristics, such as permeability, wall shear stress, and surface-to-volume ratio. Then by comparing them with the properties of Cancellous bone, the most desirable scaffolds for bone cell growth have been selected. Nine porous triply periodic minimal surfaces scaffolds in the exact unit cell sizes in four porosities have been designed. Because of the implantation of scaffolds in the body, non-Newtonian fluids can lead to more realistic results. Hence, the non-Newtonian model of the blood has also been examined for comparison with the Newtonian model. The results have shown that the permeability for Newtonian fluids was dependent only on the geometry of the scaffold, and it was intrinsic. Still, in non-Newtonian blood fluid, the permeability has been several times smaller than in the Newtonian model. Also, the average wall shear stress in the non-Newtonian model of blood has been almost twice as large as in the Newtonian model. Finally, by considering the permeability of Cancellous bones (5.13×10^{-9} m^2), scaffolds which effectively mimicked the characteristics of this type of bone have been identified. The Fischer-Koch S scaffold has the highest permeability among these four scaffolds, and Schwartz Diamond 2 scaffold has the closest permeability to Cancellous bone. This proved that selecting the most desirable scaffold is complex and challenging and should be chosen according to its conditions and application.

Review History:

Received: Sep. 13, 2021
Revised: Jan. 08, 2022
Accepted: Feb. 06, 2022
Available Online: Jun. 09, 2022

Keywords:

Triply periodic minimal surfaces scaffold
Permeability
Wall shear stress
Newtonian and non-Newtonian fluid

1- Introduction

Today, bone diseases are more important due to the increase in life expectancy in humans. Therefore, the demand for organ transplants and new artificial tissue replacements has increased. The market for orthopedic biomaterials in the United States was almost $3.4 billion in 2012. Another study affirms that 1g of bone graft substitutes costs approximately 100 USD, and the volume of materials is estimated close to 10 tons per year in 2010. The European market for bone graft substitute products for spinal fusion was valued at USD 177 million in 2010, and its growth rate is projected close to 17% per year. So, Porous scaffolds are one of the best candidates for bone replacement materials [1, 2]. These scaffolds must have different biological properties (such as permeability and wall shear stress) and structural properties (such as the surface-to-volume ratio of scaffolds) [3-7]. Biologically, scaffolds must allow the mass transfer of nutrients, oxygen, and waste metabolic products within the structure, which is related to scaffold permeability and depends on the geometry of the porous structure [3, 7]. One of the other essential parameters is the wall shear stress of the scaffolds, which is the main factor in controlling the amount of cell deposition and is strongly influenced by the network structure of the scaffold pores [8]. In addition to the items mentioned, porous scaffolds should have a large surface area to increase the possibility of cell adhesion and proliferation. Scaffolds should also provide a suitable microenvironment for cell growth and proliferation and have interconnected pores to prevent and inhibit mass transfer and cell migration [3, 7]. As it was observed, most of the scaffold characteristics are determined by the scaffold topology, so choosing the suitable unit cell is very important. In recent years, the design trend of scaffolds has changed from traditional (such as Cube) to Triply Periodic Minimal Surfaces (TPMS) based (such as Gyroid). For TPMS scaffolds have a high surface-to-volume ratio, zero mean curvature, and ease of functional grading. Traditional scaffolds have sharp convex edges and corners that prevent cell attachment and proliferation in these areas [1, 6, 9].

Extensive research has been done on the parameters affecting bone growth. The results of Castro et al. [7] showed that the unit cell design significantly impacts the calculated permeability and fluid flow velocity, regardless of the same porosity. Yongtao et al. [1] showed that structures with simple and direct pores had higher permeability than structures with complex pores. Other studies on the effect of porosity and pore size on permeability have been performed through experimental and numerical experiments. The results of Dias et al. [10] and Ma et al. [11] showed that permeability increases with increasing porosity and pore size. Also, they pointed out that the roughness of surfaces of scaffolds could influence transmission performance, especially for scaffolds

*Corresponding author's email: khavasi@znu.ac.ir

with small pore sizes. Davar and Sen [12] also showed that high porosity increases permeability and reduces wall shear stress. Zhianmanesh et al. [13] investigated the permeability numerically and experimentally and showed good agreement in the permeability results of Computational Fluid Dynamics (CFD) and experiments. Another study was performed on the effect of non-Newtonian flow on permeability and wall shear stress. Davar and Sen [14] concluded that the permeability in Newtonian fluids was several times higher than in non-Newtonian fluids. The wall shear stress in the non-Newtonian fluid was almost twice as large as a Newtonian fluid. They also mentioned that this difference in wall shear stress is due to their viscosity behaviors. Zhang et al. [15] investigated that the graded samples compared to uniform samples could flexibly control the structural parameters. Callens et al. [16] proposed a parametric design strategy for metamaterials that could tune effective permeability and elastic properties independently. They used hyperbolic tile theory to develop simple patterns according to which TPMS is divided into hard and soft regions. Through computational analysis, they showed that the arrangement of hard, soft, and porous phases in TPMS significantly increases their permeability-elasticity. In constant permeability, they have high adjustability in elastic and anisotropy properties.

Despite extensive research devoted to the mechanical and functional properties of scaffold fluid flow, most numerical studies have been performed on traditional scaffolds such as cubes or certain types of TPMS structures like Gyroid. There have also been few studies comparing TPMS scaffolds with Cancellous bone and selecting the most desirable scaffold. Therefore, the present study investigates the effect of unit cell type in different porosities on bone growth characteristics such as permeability, wall shear stress, and the surface-to-volume ratio. So in this study, due to the diversity of TPMS structures, nine TPMS scaffolds were designed in four porosities (60%, 70%, 80%, and 90%) and exact unit cell sizes, unlike the other studies. This means that in other studies, structures were designed by determining pore size at a constant thickness. That caused the size of the unit cell to change and the structure to become larger with increasing porosity. This design process can be problematic in some cases where different porosities of constant size are required. Also, their permeability and wall shear stress were compared for both Newtonian and non-Newtonian fluids. In addition to the above, a comparison has been made with human Cancellous bone to select the most desirable scaffold for implantation in the body in terms of permeability, the wall shear stress distribution, and the surface-to-volume ratio.

The process of the present work is as follows: in section 2, the scaffolds, the governing equations, and conditions of the problem are stated; The results are reported in section 3 and discussed and concluded in sections 4 and 5, respectively.

2- Materials and Methods

2- 1- Scaffold models

In this study, programming software has been used to design TPMS scaffolds. The nine TPMS scaffolds include Gyroid, Fischer-Koch S, F-RD, I-WP, Lidinoid, Neovius, Schwarz-diamond, Schwarz-diamond 2, and Schwarz-primitive, as shown in Fig. 1, in four porosity (60%, 70%, 80%, and 90%) are designed. As a result, 36 models were created. The reason for choosing these four porosities is the ability of bone to grow in porosities larger than 50% [17]. These scaffolds are designed in a cube with a length of $10\,\mathrm{mm}$. The equations of TPMS architecture are listed in Table 1, and the geometric properties of the scaffolds, such as porosity (ϕ), thickness (T), and surface-to-volume ratio (S/V), are listed in Table 2. The scaffolds are designed to be $2\times2\times2$ with a unit cell size of $5\,\mathrm{mm}$ and homogeneous. After being designed and saved in .stl format, these scaffolds are sent to design software to correct design errors such as open corners, intersecting faces, non-manifold edges, etc.

In equations related to TPMS structures which are mentioned in Table 1, C is a constant parameter that controls the amount of volume fraction of unit cell. Also, x, y, and z are defined as follows:

$$m=\frac{n_m \pi X}{L_m} \tag{1}$$

In Eq. (1), m denotes the x, y, and z directions. Also, n_m and L_m indicate the number and size of unit cells in each direction [18].

2- 2- Governing equations

2- 2- 1- Permeability

The permeability (k) of a porous medium is determined based on the Darcy relation as follows [10]:

$$k=-\frac{\mu Q}{A(\Delta P/\Delta L)} \tag{2}$$

Where μ, Q, A, ΔP and ΔL are the fluid viscosity ($\mathrm{Pa.s}$), the volumetric flow rate ($\mathrm{m^3/s}$), the inlet cross-section ($\mathrm{m^2}$), the pressure difference at the inlet and outlet or the pressure drop (Pa), and the distance between the inlet and outlet of the porous medium (m), respectively. A negative sign indicates the direction of pressure in the positive direction of the z axis. Also, the ratio Q/A is the Darcy velocity which is defined as the flow per unit cross-sectional area of the porous medium [4]. It should be mentioned that Darcy's law is valid for laminar flow, incompressible flow, steady flow, creeping flow, one-way flow, constant temperature, and the porous medium through which the fluid passes must be homogeneous [4, 23].

Because bone is a vascular tissue, all the blood vessels across the fracture line rupture when broken, blood then flows from the torn arteries to the gap between the broken bone. Therefore, it can be concluded that blood flow is distributed to its pores in the first stage of scaffold implantation. According-

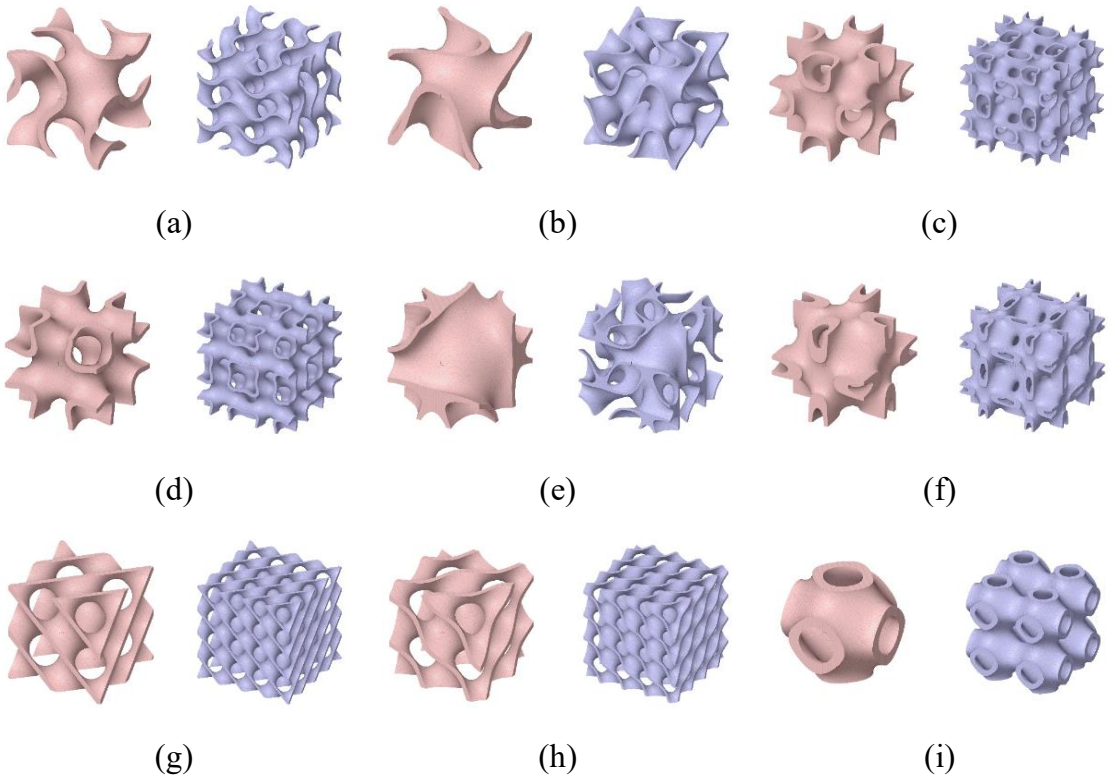

Fig. 1. Three-dimensional schematic of unit cells (red) and scaffolds based on TPMS (blue), a) Gyroid, b) Fischer-Koch S, c) F-RD, d) I-WP, e) Lidinoid, f) Neovius, g) Schwarz-diamond, h) Schwarz-diamond 2 and i) Schwarz-primitive

Table 1. Parametric equations for TPMS structures [1, 14, 19-22]

TPMS architecture	Equations
Gyroid	$cos(2x).sin(2y)+cos(2y).sin(2z)+cos(2z).sin(2x)=C$
Fischer-Koch S	$[cos(2x).sin(y).cos(z)]+[cos(x).cos(2y).sin(z)]+[sin(x).cos(y).cos(2z)]=C$
F-RD	$3[cos(x)+cos(y)+cos(z)]+8[cos(x).cos(y).cos(z)]=C$
I-WP	$2[cos(x).cos(y)+cos(y).cos(z)+cos(z).cos(x)]-[cos(2x)+cos(2y)+cos(2z)]=C$
Lidinoid	$\frac{1}{2}[sin(2x).cos(y).sin(z)+sin(2y).cos(z).sin(x)+sin(2z).cos(x).sin(y)]-$ $-\frac{1}{2}[cos(2x).cos(2y)+cos(2y).cos(2z)+cos(2z).cos(2x)]=C$
Neovius	$3[cos(x)+cos(y)+cos(z)]+4[cos(x).cos(y).cos(z)]=C$
Schwarz-diamond	$sin(x).sin(y).sin(z)+sin(x).cos(y).cos(z)+cos(x).sin(y).cos(z)+cos(x).cos(y).sin(z)=C$
Schwarz-diamond 2	$sin(x).sin(y).sin(z)+sin(x).cos(y).cos(z)+cos(x).sin(y).cos(z)+$ $+cos(x).cos(y).sin(z)+cos(x).cos(y).cos(z)=C$
Schwarz-primitive	$cos(x)+cos(y)+cos(z)=C$

Table 2. Geometric properties of scaffolds

Scaffolds	ϕ (%)	T (mm)	S/V (mm^{-1})
Gyroid	60.43	0.71	3.41
	70.30	0.53	4.50
	80.08	0.36	6.60
	89.86	0.19	12.64
Fischer-Koch S	60.42	0.75 ± 0.16	2.98
	70.46	0.56 ± 0.12	3.39
	80.41	0.37 ± 0.08	5.88
	90.34	0.19 ± 0.04	11.63
F-RD	60.18	0.40 ± 0.12	3.70
	70.23	0.35 ± 0.14	5.07
	79.84	0.23 ± 0.09	7.52
	90.10	0.11 ± 0.06	15.21
I-WP	60.17	0.63 ± 0.11	3.72
	70.31	0.46 ± 0.08	5.01
	80.26	0.31 ± 0.06	7.49
	89.59	0.16 ± 0.03	14.01
Lidinoid	60.02	0.48 ± 0.08	3.15
	70.30	0.35 ± 0.05	4.31
	79.68	0.23 ± 0.04	6.30
	89.60	0.11 ± 0.01	12.20
Neovius	69.83	0.77 ± 0.45	4.58
	80.09	0.49 ± 0.269	7.24
	89.87	0.25 ± 0.15	14.52
Schwarz-diamond	59.71	0.58	4.00
	69.68	0.43	5.32
	80.45	0.27	8.19
	89.60	0.14	15.17
Schwarz-diamond 2	59.83	0.58 ± 0.09	4.05
	70.00	0.41 ± 0.05	5.43
	80.12	0.27 ± 0.03	8.13
	90.30	0.13	16.40
Schwarz-primitive	59.97	1.10 ± 0.13	2.63
	70.30	0.79 ± 0.09	3.49
	80.05	0.51 ± 0.05	5.09
	89.81	0.26 ± 0.03	9.65

* The geometrical properties of Neovius scaffold in 60% porosity are not mentioned due to the lack of pores in its structure.

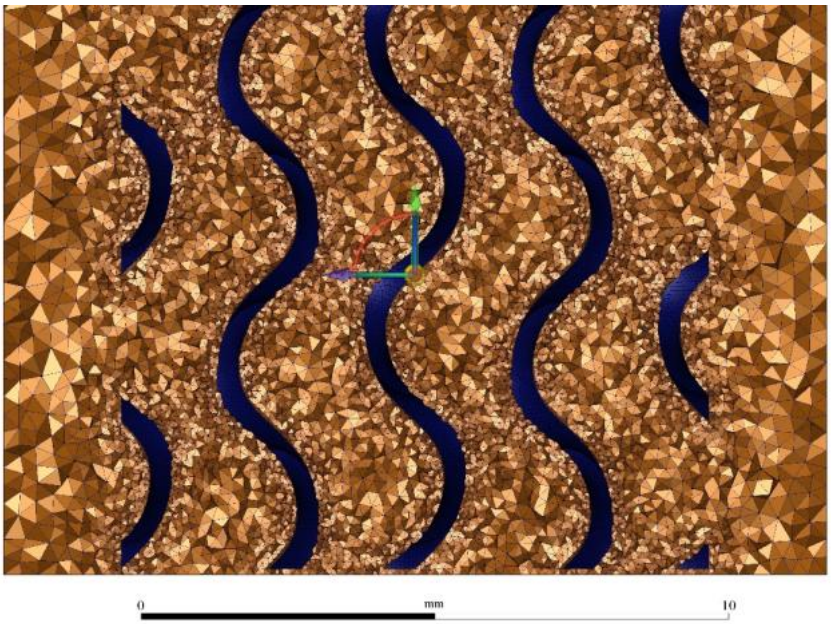

Fig. 2. An example of an acceptable mesh

ly, it is expected that more realistic results will be provided by considering the properties of blood fluid in the dynamic analysis of fluid flow in scaffolds. Modeling blood as a Newtonian fluid is a common way to simplify the parametric study of blood behavior. However, components such as cells, proteins, and ions cause non-Newtonian behavior in the blood. Due to this behavior, blood is generally known as a shear-thinning fluid [14]. To investigate the non-Newtonian fluid in this study, the the power-law model was used to calculate the viscosity.

$$\mu = K\gamma^{n-1}, \qquad \mu_{min} < \mu < \mu_{max} \tag{3}$$

K, γ and n are the consistency index ($\mathrm{Pa.s^n}$), shear rate ($\mathrm{s^{-1}}$), and flow behavior index ($n = 1$, $n > 1$, and $n < 1$ refer to the viscosity of a Newtonian fluid, shear-thickening fluid, and shear-thinning fluid, respectively), respectively. $\mu_{\min}$ and $\mu_{\max}$ are also the lower and upper cutoffs of viscosity, respectively. Therefore, the modified permeability for non-Newtonian fluid is obtained as follows [14]:

$$k = \frac{Q}{A} K \left(\frac{\Delta L}{\Delta P}\right)^{1/n} \tag{4}$$

2- 2- 2- Wall shear stress

In a laminar flow, Wall Shear Stress (WSS) (τ_w) can be defined as the normal velocity gradient on a wall. Therefore, the wall shear stress for a Newtonian model is obtained from the following equation:

$$\tau_w = \mu \frac{\partial u}{\partial m} \tag{5}$$

where u and m refers to the flow velocity and wall-normal direction, respectively [14]. Also, In the non-Newtonian model, the wall shear stress is defined as follows [24]:

$$\tau_w = K \left(\frac{\partial u}{\partial m}\right)^n \tag{6}$$

2- 3- Numerical simulation

The fluid domain of all designed models is meshed using tetrahedral elements. Fig. 2 shows an example of an acceptable mesh. To increase the reliability of the simulation, some computations are provided for the independence of the results from the mesh topology by refining the mesh. Therefore, a grid sensitivity study was performed in four different levels for Gyroid, F-RD, and Neovius scaffolds designed in 80% porosity and similar conditions. The results of this study are reported in Table 3. As can be seen, the number of elements increased by a factor of approximately 1.8. However, the difference in the permeability and average wall shear stress results in the F-RD and Neovius models in numbers 1 and 2 was more than 5%, but in the other two numbers, 3 and 4, they reached less than 1%. Among numbers 3 and 4, mesh number 3 has been selected due to the smaller number of elements and consequently less processing and simulation time. Fig. 3 shows an example of a mesh.

Table 3. Number of elements of Gyroid, F-RD, and Neovius scaffolds in 80% porosity for mesh independence

Scaffolds	Grid number	Number of elements	Permeability ($10^{-8}m^2$)	Average wall shear stress (mPa)
Gyroid	1	983359	6.340	0.653
	2	2067790	6.282	0.662
	3	3673012	6.251	0.667
	4	6353884	6.227	0.672
F-RD	1	1162104	2.396	0.980
	2	2168156	2.341	1.009
	3	4004960	2.300	1.032
	4	7260776	2.274	1.046
Neovius	1	1040503	0.670	1.931
	2	1903496	0.649	2.010
	3	3624802	0.630	2.088
	4	6771952	0.617	2.142

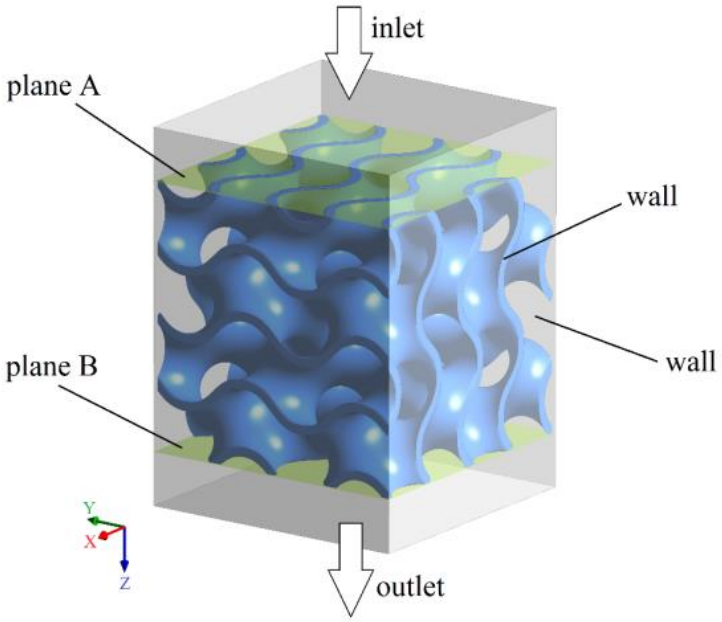

Fig. 3. Boundary conditions in numerical simulation

Also, in the rest of the scaffolds, to ensure the simulation, based on the sizes of the two grids mentioned (numbers 3 and 4), they have meshed, and their results are mentioned in Table 4. It can be seen that the difference in their permeability and average wall shear stress results is less than 1%. Therefore, from the two available meshes, similar to Table 3, the network with fewer elements (gray color) is selected for numerical simulations. The number of elements of all scaffolds in the four porosities in the simulation is presented in Table 5.

Table 4. Number of elements of remaining scaffolds in 80% porosity for mesh independence

Scaffolds	Grid number	Number of elements	Permeability ($10^{-8}m^2$)	Average wall shear stress (mPa)
Fischer-Koch S	1	3299168	7.238	0.623
	2	5551184	7.208	0.627
I-WP	1	4470948	4.379	0.792
	2	8040461	4.356	0.787
Lidinoid	1	3745400	4.980	0.740
	2	6743416	4.949	0.746
Schwarz-diamond	1	4779139	4.031	0.908
	2	9126473	4.009	0.916
Schwarz-diamond 2	1	4798928	3.742	0.939
	2	9242700	3.718	0.930
Schwarz-primitive	1	2124328	6.019	0.488
	2	3207651	5.996	0.491

Table 5. Number of elements for numerical simulation

Scaffolds	ϕ (%)			
	60	70	80	90
Gyroid	3164080	3364605	3673012	4200176
Fischer-Koch S	2425103	2816822	3299168	3767596
F-RD	2780522	3418250	4004960	4652480
I-WP	3178552	3640497	4470948	4814992
Lidinoid	2673174	3202664	3745400	4221189
Neovius		2986393	3624802	4135055
Schwarz-diamond	4060607	4346564	4779139	5047810
Schwarz-diamond 2	3981150	4339445	4798928	5113805
Schwarz-primitive	1860973	1935481	2124328	2942744

Table 6. Fluids and scaffolds selected for analysis

Fluid	Type of viscosity	Scaffold
Water	Newtonian	All scaffolds
Blood	Newtonian	Gyroid
Blood	Non-Newtonian	All scaffolds

2- 3- 1- Fluids properties

Initially, water was selected as the fluid for simplification. Then, as mentioned, in the first stage of scaffold implantation, blood flow is distributed to the pores of the scaffolds. For this reason, blood after water is considered as a non-Newtonian fluid flowing in scaffolds. Also, for better comparison, blood as a Newtonian fluid has been studied with water and non-Newtonian blood in a Gyroid scaffold. Briefly, the selected fluids in this study and their scaffolds are listed in Table 6. The density of water and blood in the Newtonian model are 1000 and 1050 $\mathrm{kg/m^3}$, respectively, and their viscosity is 0.001 and 0.004 $\mathrm{Pa.s}$, respectively. In the non-Newtonian model of blood, density, consistency index, flow behavior index, and lower and upper cutoffs of viscosity are equal to 1050 $\mathrm{kg/m^3}$, 0.017 $\mathrm{Pa.s^n}$, 0.708, 0.001 $\mathrm{Pa.s}$, and 0.1 $\mathrm{Pa.s}$, respectively [12, 14].

2- 3- 2- Boundary conditions and convergence

The inlet flow velocity is assumed to be 0.1 $\mathrm{mm/s}$ for water [12] and 0.7 $\mathrm{mm/s}$ for blood fluid. This value for blood is in the range of blood velocity (0.5-0.8 $\mathrm{mm/s}$) in the bone marrow microvessels [14]. The boundary condition of no-slip is attributed to the walls and the zero gauge pressure for the output. The deformation of the scaffolds due to the interaction of the flow and the wall has also been neglected. The boundary conditions are shown in Fig. 3. As shown in Fig. 3, the inlet is spaced from the scaffold to prevent boundary effects on the flow. Plane A is used to calculate the inlet pressure and velocity, and plane B is used to calculate the outlet pressure from the scaffold. Therefore, the pressure drop is obtained according to the following equation:

$$\Delta P = P_{plane\ A} - P_{plane\ B} \tag{7}$$

All the calculations are conducted as double-precision to determine the fluid flow more accurately. Simulations for residues less than 10^{-5} are assumed to be convergent.

3- Results

3- 1- Validation

To validate the present study, first, the models designed by Davar and Sen for Newtonian flow [12] and non-Newtonian flow [14] according to the mentioned specifications have been designed. Then, simulations are performed according to the boundary conditions, and the results presented in Fig. 4 are obtained. Fig. 4 shows a comparison diagram of a Gyroid scaffold's permeability and average wall shear stress for Newtonian and non-Newtonian fluids. As can be seen, the results obtained by Davar and Sen and the model designed based on them have an error of less than 15%, which shows a good agreement.

Also, in the present study, unlike previous studies, the structures are designed in fixed unit cell size. This means that in previous studies, by determining the size of pores at a constant thickness, they designed structures that caused the size of the unit cell to change, and thus the structure became larger with increasing porosity. This design process can be problematic in some cases where different porosities of constant size are required.

To validate this design process, permeability must be dimensionless due to the different dimensions of the structures. Therefore, the permeability of different porosities in Fig. 4, in addition to the permeability of the model designed in this study, is dimensionless by the scaffold size and is reported in Fig. 5. As can be seen, the dimensionless permeability of this study and the model designed based on Davar and Sen has an error of less than 3% and also, with their results, has an error of less than 15%. As a result, it can be said that the permeability of a type of scaffold in a Newtonian fluid depends only on the porosity of the desired geometry. In dimensionless permeability for non-Newtonian fluid, there was more than a 50% difference between the model designed in this study with the model of Davar and Sen and the model designed based on them. The reason for this difference in the non-Newtonian fluid will be explained below.

3- 2- Fluid flow dynamics

To illustrate how the velocity is distributed, its contour is shown in Fig. 6, for example, in the Gyroid model and the four porosities available for Newtonian and non-Newtonian blood fluids at an inlet velocity of 0.7 $\mathrm{mm/s}$. The velocity contour is in the mid-plane and the direction of the flow path, i.e., the positive Z axis.

As shown in Fig. 6, the velocity inside the scaffold is several times the inlet velocity, which indicates the obstruction, swirled, and acceleration of the fluid because the cross-sectional area of the channel is different from the cross-sectional area of different parts of the scaffold. As the cross-sectional area decreases, according to the conservation of mass, the velocity must increase. Also, the unique and complex architecture of the scaffold causes fluid to swirl.

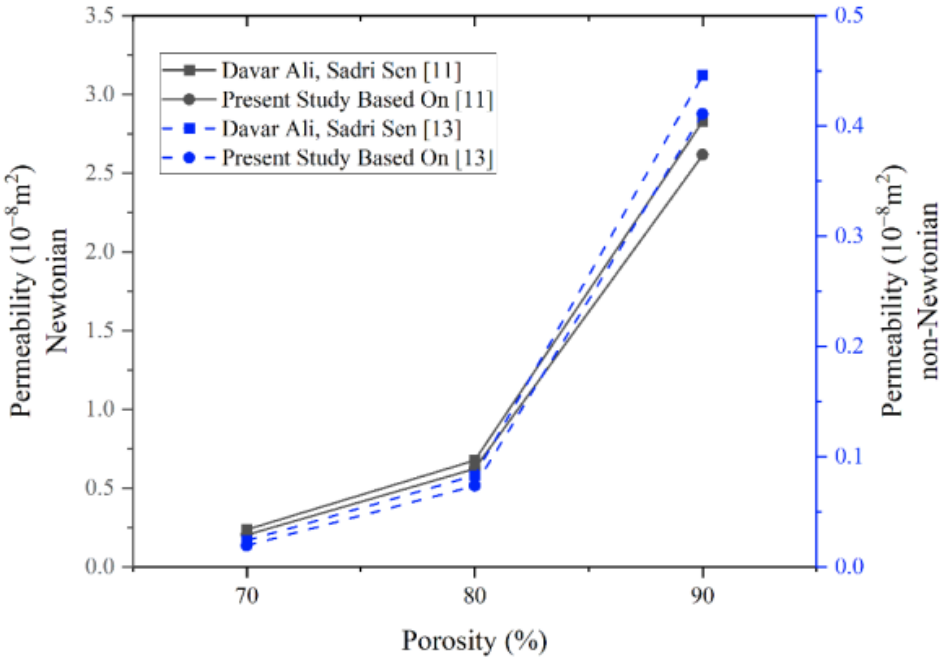

(a)

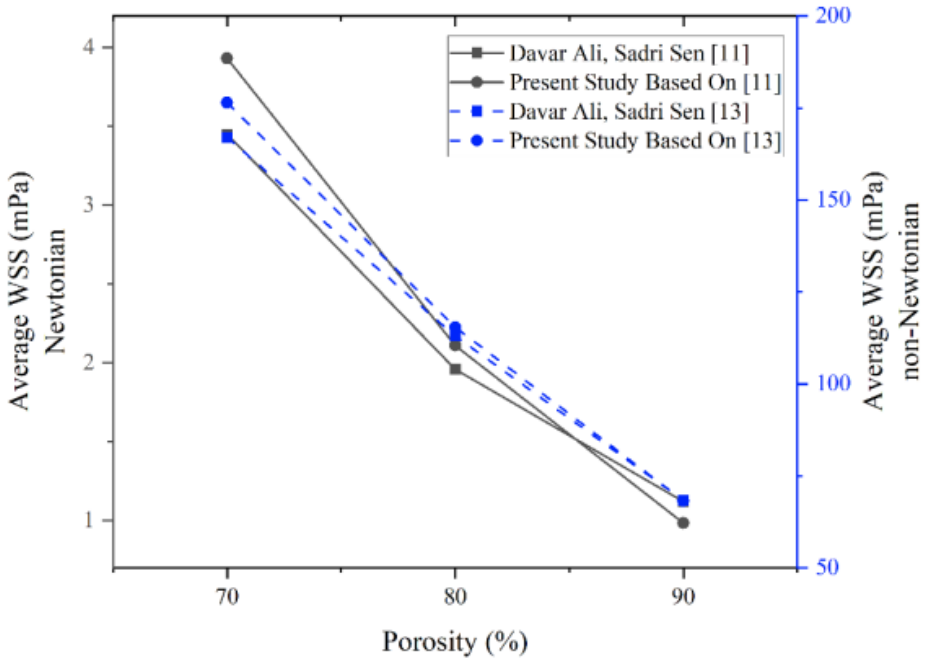

(b)

Fig. 4. Validation diagram of gyroid scaffold designed based on Davar and Sen with their results [12, 14], a) permeability and b) wall shear stress

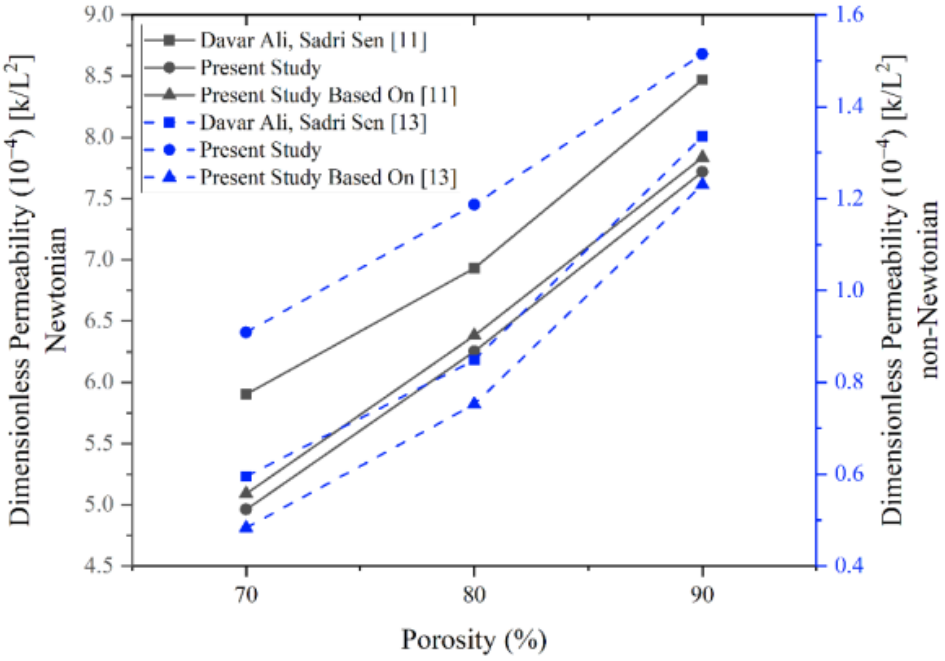

Fig. 5. Validation diagram of dimensionless permeability of Gyroid scaffold in the present study with the results of Davar and Sen [12, 14]

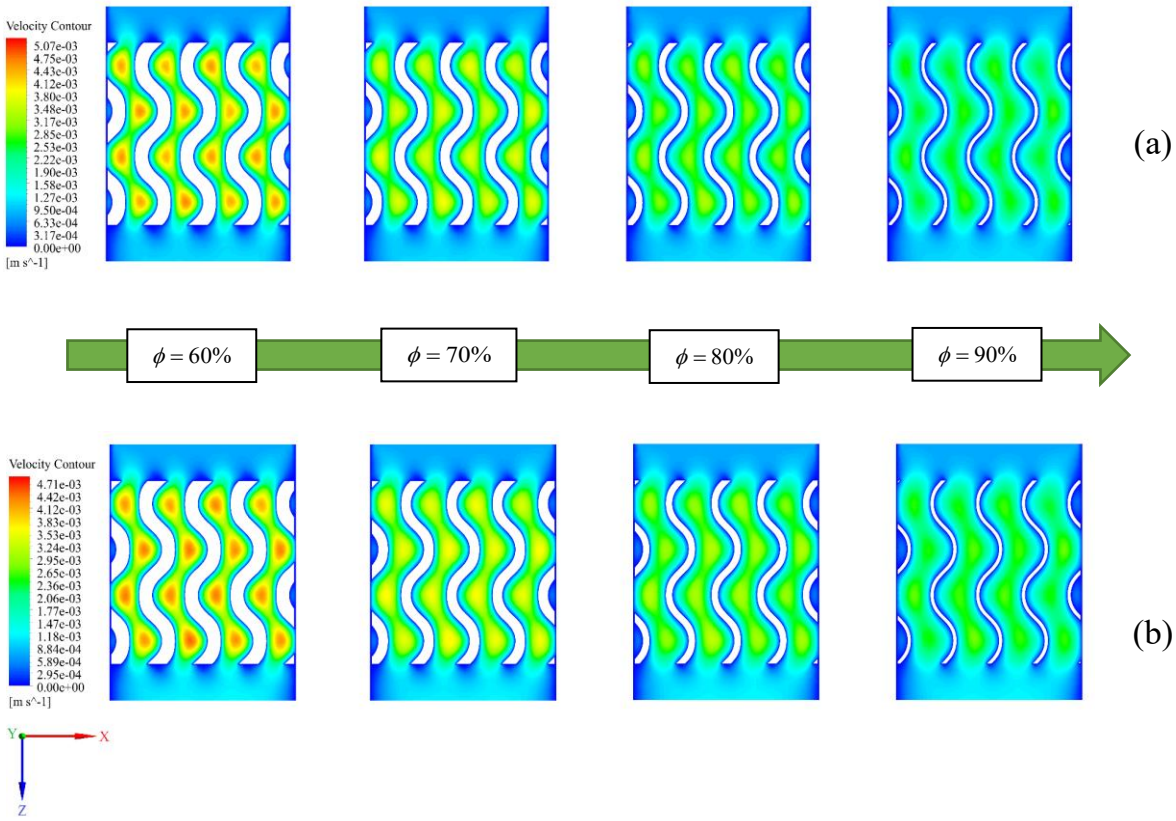

Fig. 6. Velocity contour in the mid-plane of the Gyroid scaffold, a) Newtonian blood, and b) Non-Newtonian blood

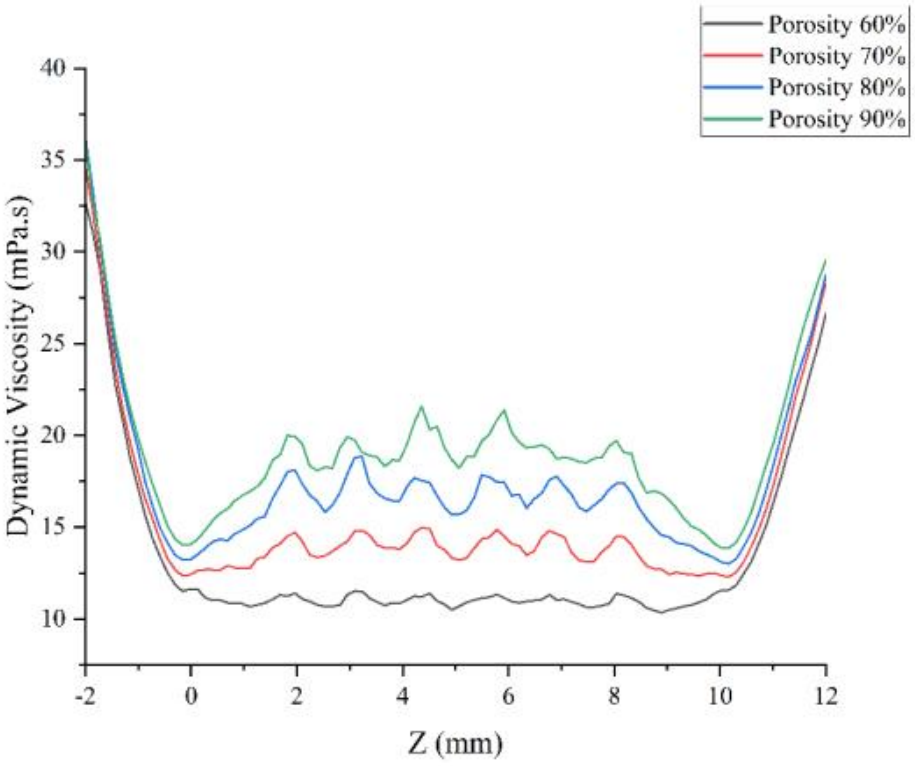

Fig. 7. Diagram of viscosity variation with location from the beginning (-2mm) to the end of the channel (12mm) in one of the pores of the Gyroid scaffold

In Fig. 6, the velocity varies decreasingly as the porosity changes from 60% to 90%, i.e., as the porosity increases, because the inlet cross-sectional area increases to keep the fluid flow constant. It is also observed that the maximum velocity in the Newtonian fluid is higher than the non-Newtonian fluid. To justify this, the trend of viscosity variation in the non-Newtonian model must be examined. As mentioned, blood is a shear-thinning fluid, i.e., its viscosity decreases with increasing shear rate. Thus, the trend of viscosity variation in the non-Newtonian model from the beginning (-2mm) to the end of the channel (12mm) in one of the Gyroid pores is shown in Fig. 7, its viscosity contour in the mid-plane is also shown in Fig. 8, and the place of calculation of these variations is shown in Fig. 9. As shown in Figs. 6 and 7, the viscosity increases with increasing porosity. Unlike the Newtonian model, viscosity does not have a constant value and changes in the fluid domain. According to Fig. 6, the velocity gradient at the beginning and end of the channel is low, which increases viscosity in these areas. Inside the scaffold, the viscosity in these areas is reduced due to the increase in velocity gradient. Also, the velocity gradient is variable due to the architectural twists and turns of the scaffold, which causes the viscosity to fluctuate inside the scaffold. Comparing the viscosity of the Newtonian and non-Newtonian models of blood, at the very least, the viscosity of the non-Newtonian model is approximately 2.5 times higher than the viscosity of the Newtonian model, which reduces the velocity of the fluid in the scaffold in the non-Newtonian model compared to the Newtonian model.

To better compare the viscosity variations in the non-Newtonian model with the variations of the geometry dimension, Fig. 10 presents a diagram of the viscosity variations with the location for the present study and the study based on Davar and Sen [14]. As mentioned and shown in Fig. 10, the viscosity in the non-Newtonian model is variable and increases with increasing porosity, i.e. the viscosity in the non-Newtonian model depends on the geometry of the scaffold with its change, the viscosity has changed. Therefore, in dimensionless permeability based on the model size or pores for the non-Newtonian model, due to the viscosity in the relationship and its dependence on geometry, the non-Newtonian permeability of this study was more than 50% different from the Davar and Sadri models.

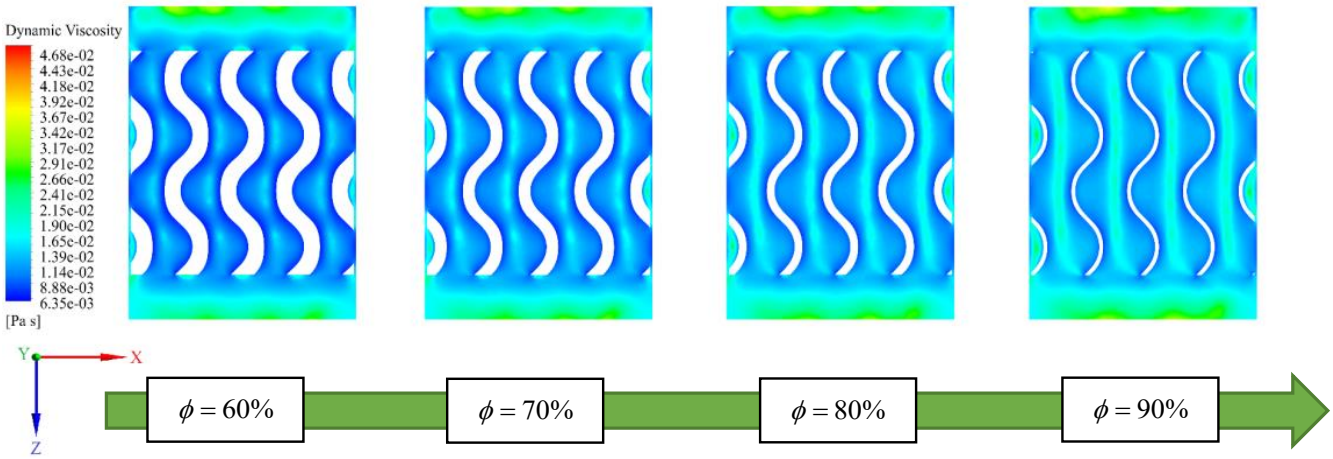

Fig. 8. Viscosity contour of a non-Newtonian model in the mid-plane of the Gyroid scaffold

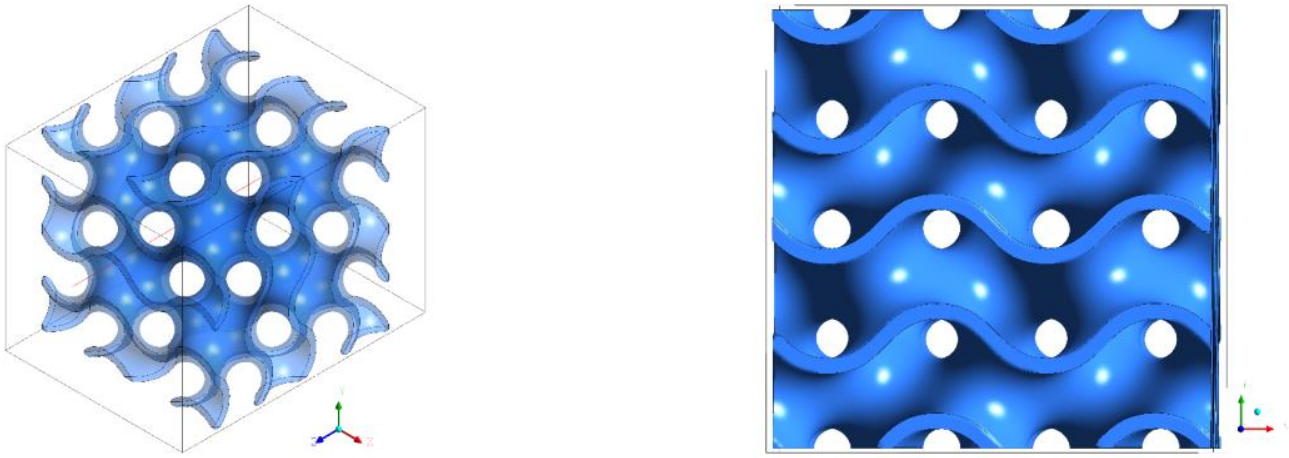

(a) (b)

Fig. 9. Location of calculation of viscosity variations with location (red line) for Gyroid scaffold in 80% porosity, a) three-dimensional view, and b) view perpendicular to the flow path

The above explanations for the velocity and viscosity contour of the Gyroid scaffold can be generalized to the rest of the mentioned scaffolds because all scaffolding has the same conditions in terms of design and simulation. To ensure this, the Darcy velocity and pressure drop of all scaffolds are plotted in Figs. 10 and 11 for both Newtonian and non-Newtonian models, respectively. It should be noted that the Darcy velocity and pressure drop in the Newtonian and non-Newtonian models are plotted for water and blood fluid at inlet velocities of 0.1 and 0.7 mm/s, respectively.

Fig. 11 shows that the descriptions of flow velocity and viscosity in the Gyroid scaffold apply to all designed scaffolds in both Newton and non-Newton models. Also, the lowest and highest Darcy velocities in both Newtonian and non-Newtonian models are related to F-RD and Lidinoid at 90% and 60% porosity, respectively.

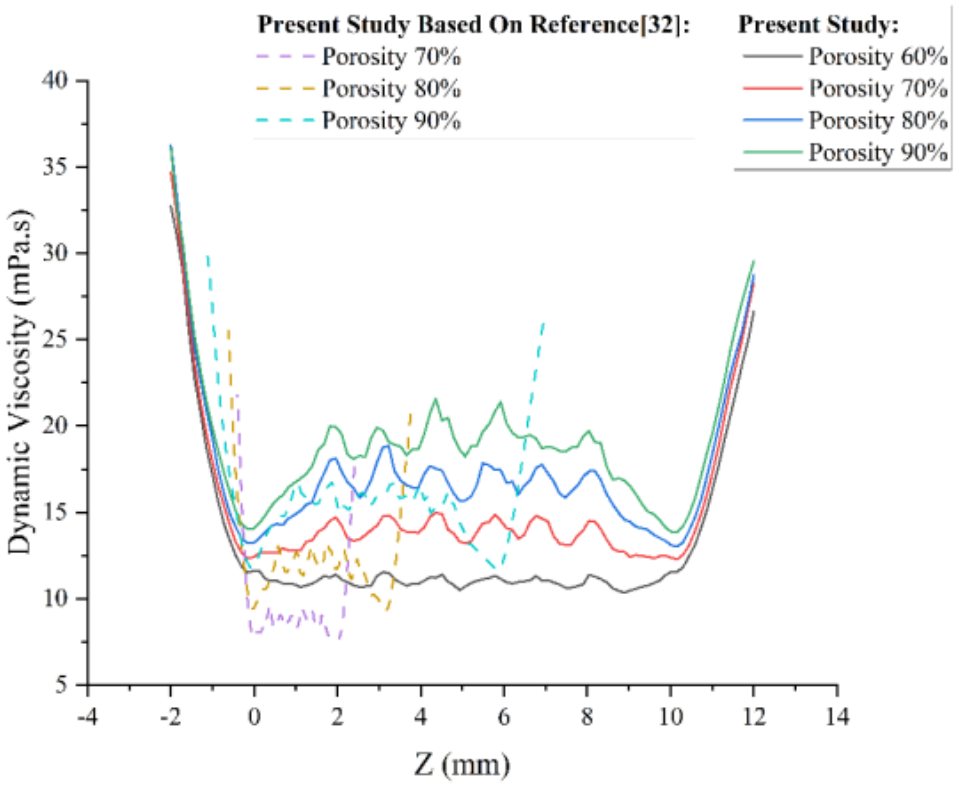

Fig. 10. Comparison of viscosity variations with the location for the present study and the study based on Davar and Sen [14]

Fig. 12 shows a diagram of pressure drop variations in all scaffolds for both Newtonian and non-Newtonian models and the four available porosities. It can be seen that in the non-Newtonian model, as well as in the Newtonian model, as mentioned for velocity, there is more resistance to flow due to increased viscosity. Therefore, under the same boundary conditions, the pressure drop in the non-Newtonian model is more significant than in the Newtonian model. As a result, the factor that makes the scaffolds under non-Newtonian modeling less permeable is the increase in pressure drop across them. The lowest and highest pressure drops are related to Fischer-Koch S and Neovius scaffolds at 90% and 70% porosity, respectively.

3- 3- Permeability

The permeability of each scaffold is calculated according to the pressure drop from the structures and using the classic and modified Darcy equation. The permeability values of the Newtonian and non-Newtonian models calculated for each scaffold are shown in Fig. 13. As can be seen, the increase in porosity in each scaffold has increased the permeability due to the decrease in pressure drop. The permeability in the Newtonian models is in the range of $0.11-9.23\times10^{-8}\,\mathrm{m}^2$ and in the non-Newtonian models in the range of $0.015-1.88\times10^{-8}\,\mathrm{m}^2$, which is at least related to the Neovius scaffold and at most to the Fischer-Koch S scaffold.

It is also observed that at 60% porosity, for example, the permeability of the gyroid scaffold was higher than the Schwarz-primitive scaffold and the I-WP scaffold was higher than the Lidinoid scaffold, but with increasing porosity, it is observed that the permeability of the Schwarz-primitive and the Lidinoid scaffolds has increased nonlinearly so that in 90% porosity, they are larger than the Gyroid and the I-WP scaffolds, respectively. As the porosity increases, the pore size increases nonlinearly, resulting in a nonlinear decrease in pressure drop. This nonlinear trend can also be seen in Fig. 12. Therefore, it cannot be said that in a porosity, if one geometric permeability was higher than the other geometry, then it had more permeability in other porosities as well.

The difference in permeability results in Newtonian and non-Newtonian models decreased with increasing porosity for the mentioned scaffolds. For example, in the Gyroid scaffold with 60% porosity, the permeability for the Newtonian model is about 5.68 times higher than for the non-Newtonian model. In the 90% porosity, this ratio is reduced to 5.1%. This

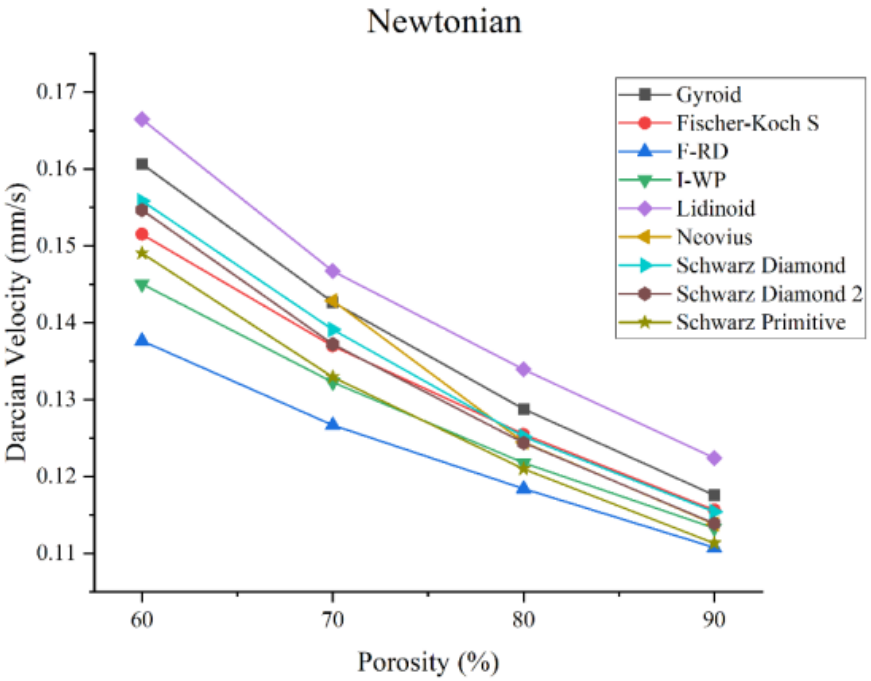

(a)

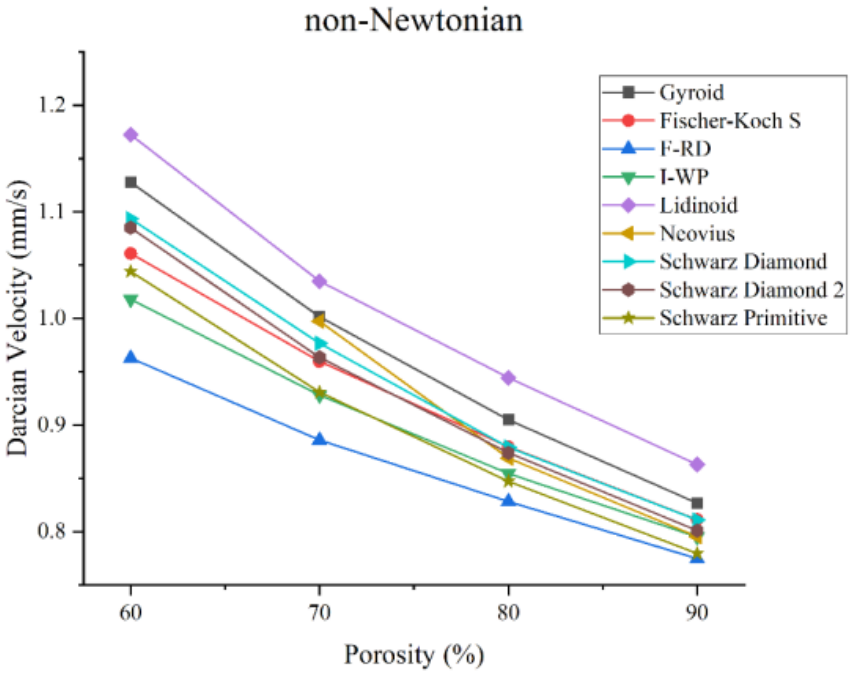

(b)

Fig. 11. Diagram of Darcy velocity variations in all scaffolds, a) Newtonian model for water fluid at 0.1 inlet velocity and b) Non-Newtonian model for blood fluid at 0.7 mm/s velocity

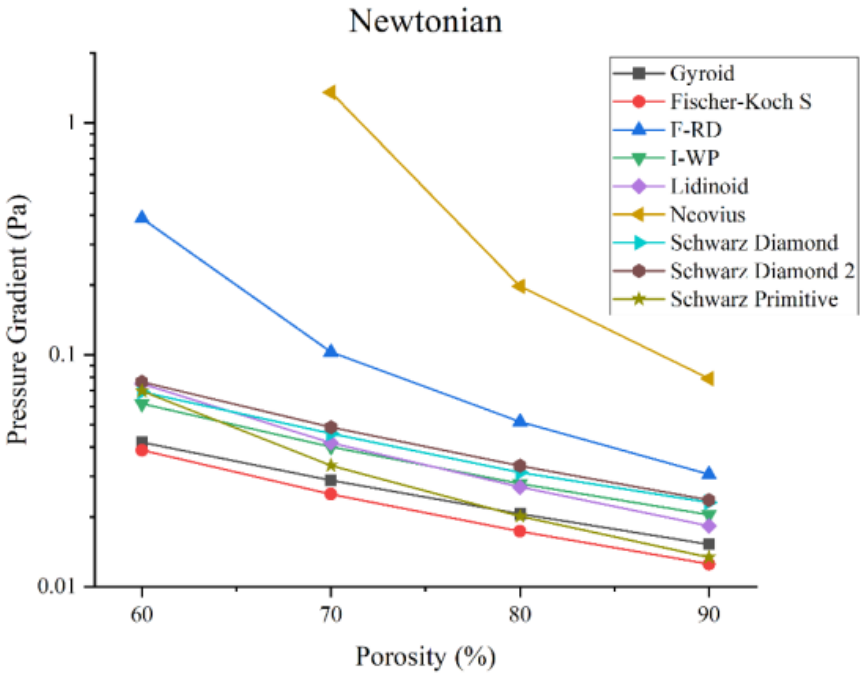

(a)

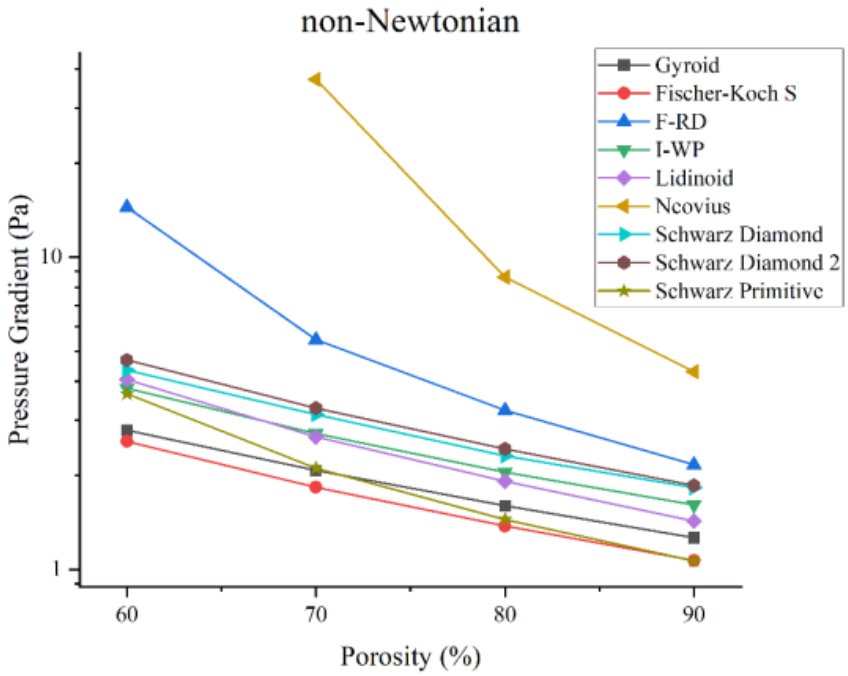

(b)

Fig. 12. Diagram of pressure drop variations in all scaffolds, a) Newtonian model for water fluid at 0.1 inlet velocity and b) Non-Newtonian model for blood fluid at 0.7 mm/s velocity

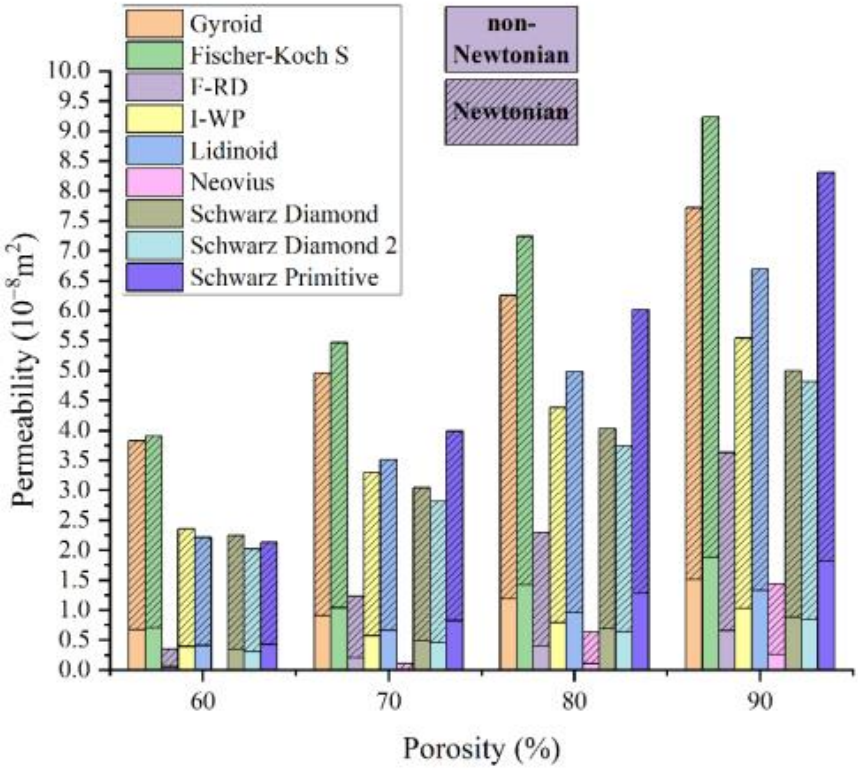

Fig. 13. Comparison diagram of the permeability results of Newtonian and non-Newtonian models of all scaffolds

reduction in the difference in the permeability results of the Newtonian and non-Newtonian models in Fig. 14 is clearly visible. As a result, it can be said that by increasing the porosity and facilitating the flow of fluid through the scaffolds, the behavior of non-Newtonian models approaches Newtonian models.

3- 4- Wall shear stress

The wall shear stress contour is presented as an example for the Gyroid scaffold in four porosities for the Newtonian and non-Newtonian models of blood at an inlet velocity of 0.7 mm/s in Fig. 15. According to Eq. (5), the wall shear stress is directly related to the velocity and viscosity gradients. Therefore, it is observed that the maximum wall shear stress occurs in areas where the scaffold is narrowed and due to which the velocity of fluid flow is increased. Therefore the maximum wall shear stress is spread in different areas of the scaffold. Also, the wall shear stress decreases with increasing porosity in both models as the pores become larger. In the non-Newtonian model, the wall shear stress is approximately twice that of the Newtonian model, so the viscosity or shear rate in the non-Newtonian model is higher than in the Newtonian model. As mentioned before, the viscosity in the non-Newtonian model was at least 2.5 times that of the Newtonian model.

Since the velocity gradient in scaffolds depends on the channel inlet velocity, the wall shear stress, unlike permeability, will vary in a fixed geometry and at different inlet velocities. Therefore, the average wall shear stress comparison in both Newtonian and non-Newtonian models is performed only for the Gyroid scaffold and for blood fluid at an inlet velocity of 0.7 mm/s and can be seen in Fig. 16. Also, the comparison of all scaffolds' average wall shear stress for the Newtonian model in water fluid at an inlet velocity of 0.1 mm/s and the non-Newtonian model in the blood fluid at an inlet velocity of 0.7 mm/s is shown in Fig. 17. As the porosity increases, as mentioned and can be seen in Figs. 15 and 16, the average wall shear stress decreases.

In Fig. 16, the average wall shear stress in the non-Newtonian model is approximately twice that of the Newtonian model for the Gyroid scaffold. It is consistent with the results reported by Davar and Sen [14].

According to Fig. 17, the average wall shear stress in the Newtonian models was in the range of $0.41-5.35mPa$ and in the non-Newtonian models $33.38-165.30mPa$, which is at least related to the Schwarz-primitive scaffold and maximum to the Neovius scaffold. It can be seen that the maximum permeability value related to the Fischer-Koch S scaffold does not have the lowest average wall shear stress. Therefore, it should not be assumed in TPMS structures that

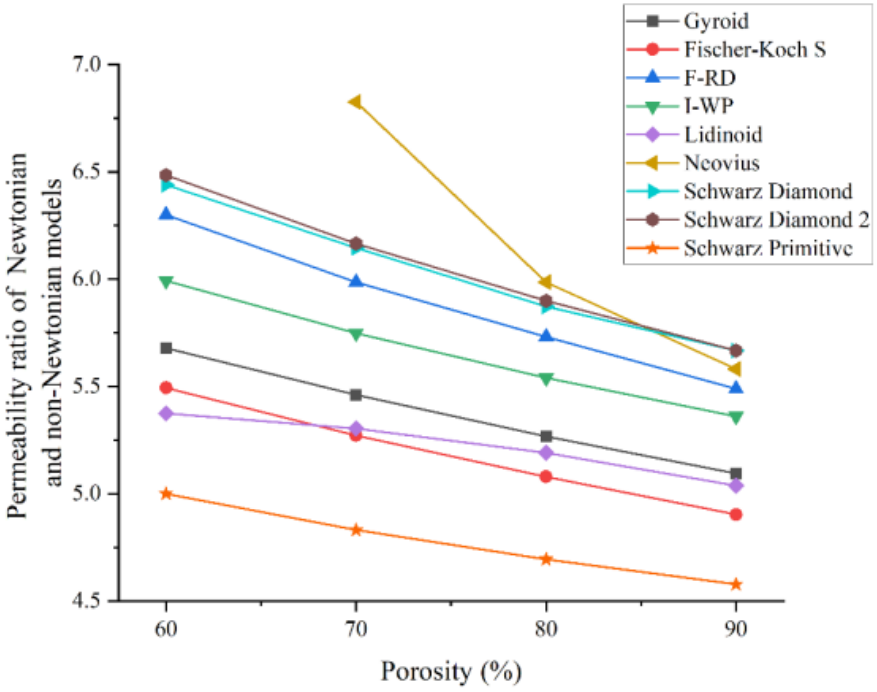

Fig. 14. Diagram of the permeability ratio of Newtonian and non-Newtonian models

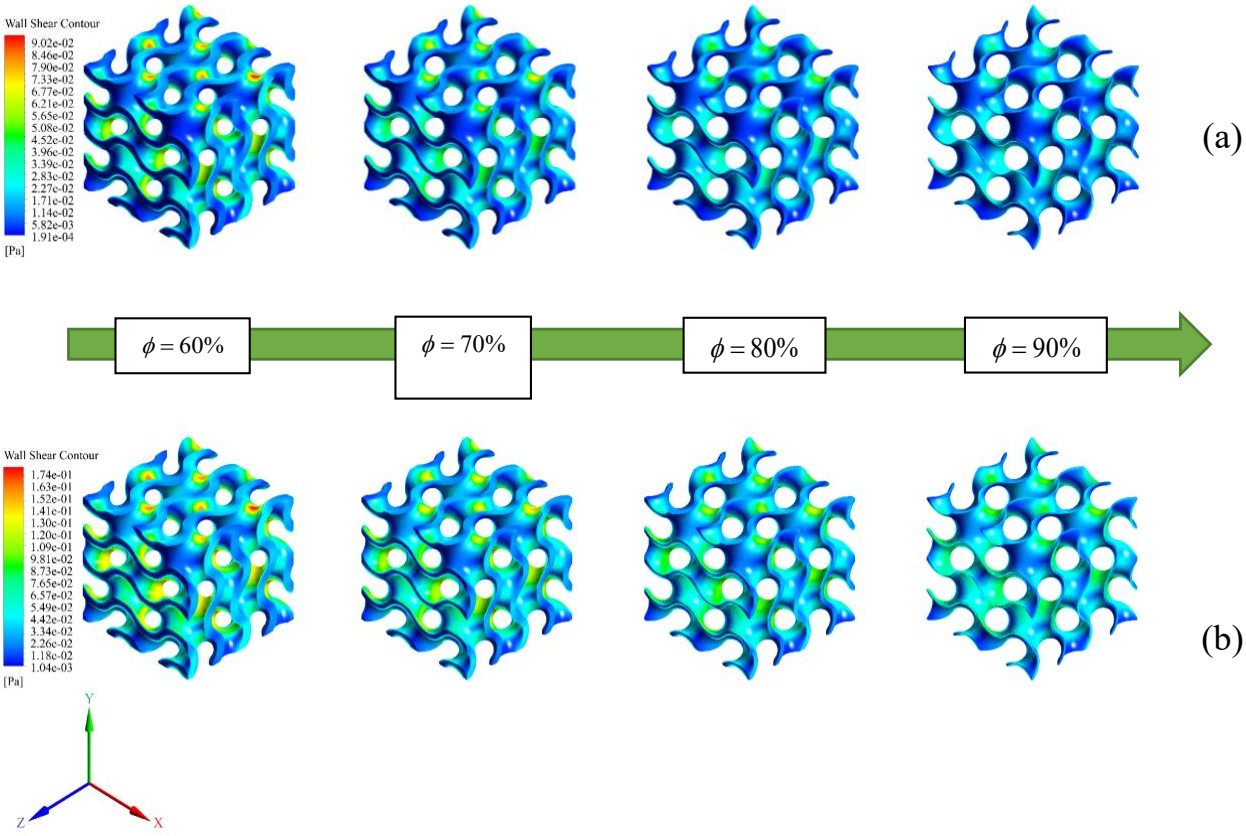

Fig. 15. Wall shear stress contour in gyroid scaffold, a) Newtonian blood and b) Non-Newtonian blood

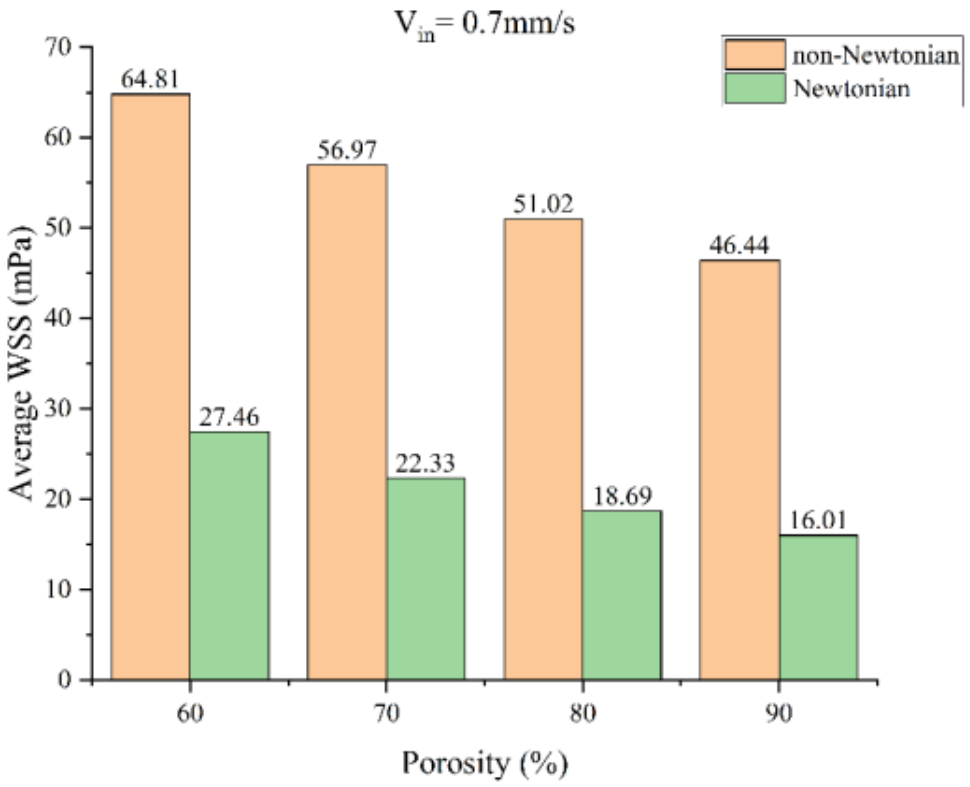

Fig. 16. Comparison diagram of average wall shear stress of the Gyroid scaffold for blood fluid in Newton and non-Newton model at 0.7 mm/s inlet velocity

if the geometry is more permeable, it must have a lower average wall shear stress because, as can be seen in Fig. 11, the Darcy velocity variation was nonlinear, so the pore size and thickness of these structures changed nonlinearly, causing nonlinear variations of velocity within the scaffolds with porosity changes.

3- 5- Surface-to-volume ratio

As mentioned, one of the advantages of TPMS structures over traditional network-based structures is the higher surface-to-volume ratio. The surface-to-volume ratio of porous scaffold depends on the size of the pores. Increasing the surface area means more exposure to the environment to interact more with the environment, i.e., a large surface area increases the possibility of adhesion and proliferation of cells. At the same time, a large pore volume is required to provide a sufficient cell population for the repair or regeneration process. Also, a lower surface-to-volume ratio is expected to achieve better mechanical integrity. Thus, there is a need to design scaffolds in different surface-to-volume ratios. Therefore, the diagram of the surface variation of scaffolds with porosity is presented in Fig. 18.

The reason for representing the surface variation of the scaffolds instead of the surface-to-volume ratio is that the scaffolds are designed in the exact dimensions of the unit cell, so they have the same volumes in the same porosity.

Fig. 18 shows that the scaffolds' surface variations with increasing porosity had an upward or downward trend. Usually, the surface of the scaffolds should change downward with increasing porosity because as the porosity increases, as mentioned in the previous sections, the pore size increases, and the thickness decreases. While in some scaffolds, with increasing porosity, the path of the scaffold pores changes from linear to nonlinear, i.e., the number of scaffold twists and bends increases, which increases the surface of the scaffold. Therefore, these nonlinear changes in pore size in some scaffolds have caused the pressure drop in them to change nonlinearly, which has ultimately made the permeability nonlinear. It is also observed that the Schwarz-diamond 2 scaffold has the highest surface area compared to other scaffolds in the same volumes, so cell adhesion and proliferation will be more effective in that.

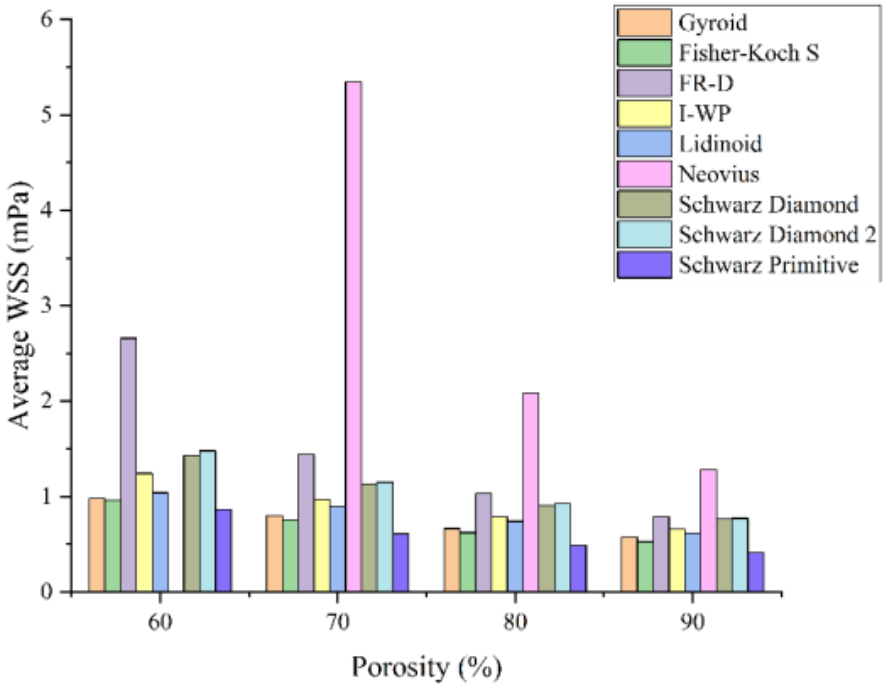

(a)

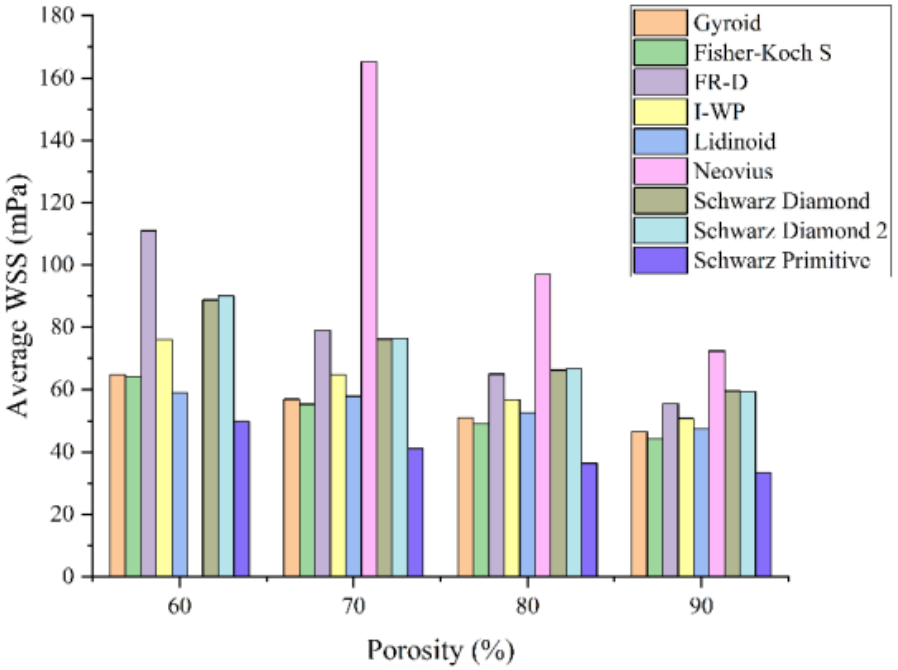

(b)

Fig. 17. Comparison diagram of the average wall shear stress results in all scaffolds for a) water fluid at 0.1 mm/s inlet velocity and b) non-Newtonian blood fluid at 0.7 mm/s inlet velocity

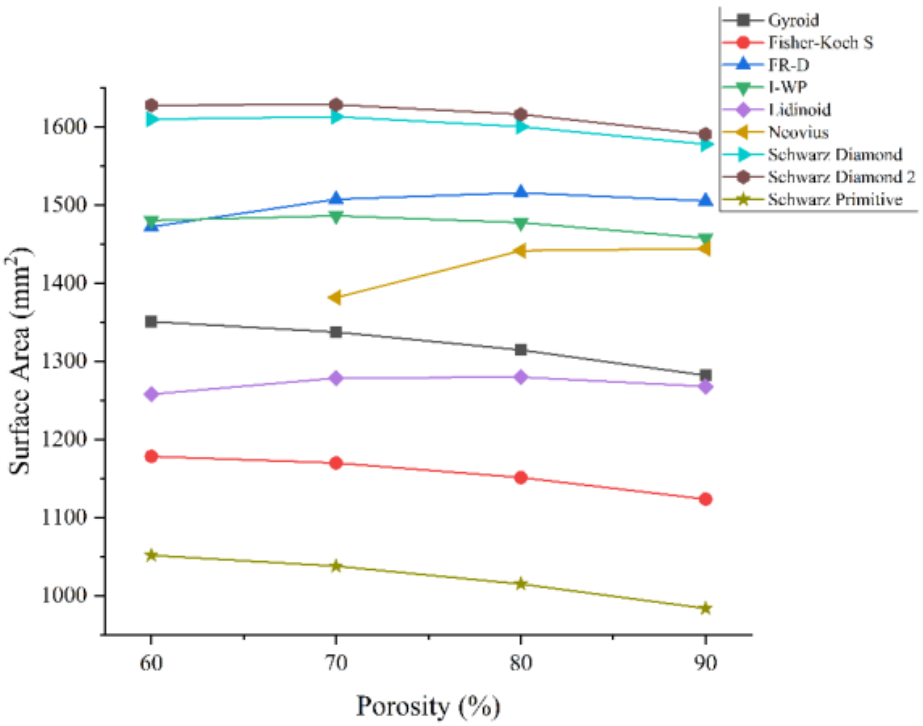

Fig. 18. Diagram of the surface variation of the scaffolds with porosity variation

4- Discussion

The permeability range of designed scaffolds should be determined based on natural human bone, as they act as scaffold hosts. The permeability of human Cancellous bone has been determined to be $5.13\times10^{-9}\,m^2$ [12], which can be used as a basis for determining the optimal scaffold. As mentioned, in the first stage of scaffold implantation, blood flow is distributed to its pores. Therefore, to realistically compare the permeability results of scaffolds designed with human Cancellous bone, the permeability of scaffolds in the non-Newtonian model of blood is compared with Cancellous bone in Fig. 19.

Fig. 19 shows that the permeability of Gyroid and Fischer-Koch S scaffolds in all porosities, I-WP, Lidinoid, and Schwarz-primitive scaffolds in porosities above 60%, Schwarz-diamond and Schwarz-diamond 2 scaffolds in porosities above 70%, and F-RD scaffolds in 90% porosity were higher than Cancellous bone permeability And met the requirements of Cancellous bone permeability. It can also be seen that the Neovius scaffold has not been able to achieve Cancellous bone permeability in any porosity.

Wall shear stress is one of the main factors controlling the amount of cell deposition and is strongly influenced by the pore network structure of the scaffolds. Therefore, the heterogeneous distribution of wall shear stress causes non-uniform cell proliferation and differentiation in scaffolds. Therefore, to restrict these scaffolds again, the statistical parameters of the Skewness and the Coefficient of Variation (CV) of the wall shear stress in each scaffold have been calculated and presented in Fig. 20. These figures showed that each of the scaffolds has a different wall shear stress distribution. It is also observed that the wall shear stress distribution can be drastically different by changing the porosity in the fixed geometry. Differences in wall shear stress distribution and wall shear stress changes with channel inlet velocity make it impossible to find a relationship between scaffolds architecture and wall shear stress distribution statistics, meaning that designing scaffolds based on optimal wall shear stress distribution is a difficult task in tissue engineering.

The value of non-zero Skewness indicates that the wall shear stresses greater than or less than the average wall shear stresses are not symmetrically distributed. Therefore, using this value in all scaffolds, it is possible to understand the symmetry of the wall shear stress distribution. As a result, the Skewness of the scaffolds in the available porosities is shown in Fig. 20-a. As can be seen, the Fischer-Koch S scaffold has the most desirable Skewness in all porosities, and its value closest to zero is -0.02 in 70% porosity.

The coefficient of variation is an indicator that can compare the wall shear stress distribution in each scaffold. The coefficient of variation greater than zero indicates the non-uniform distribution of wall shear stress in the scaffolds, so the closer the coefficient of variation is to zero, the more uniform the distribution. Therefore, the coefficient of variation of scaffolds in the available porosities in Fig. 20-b is presented. As can be seen, the Schwarz-diamond scaffold has the smallest coefficient of variation compared to other scaffolds, equal to 0.117. It has a porosity of 90%, so this scaffold has more .uniform wall shear stress than other scaffold other scaffolds

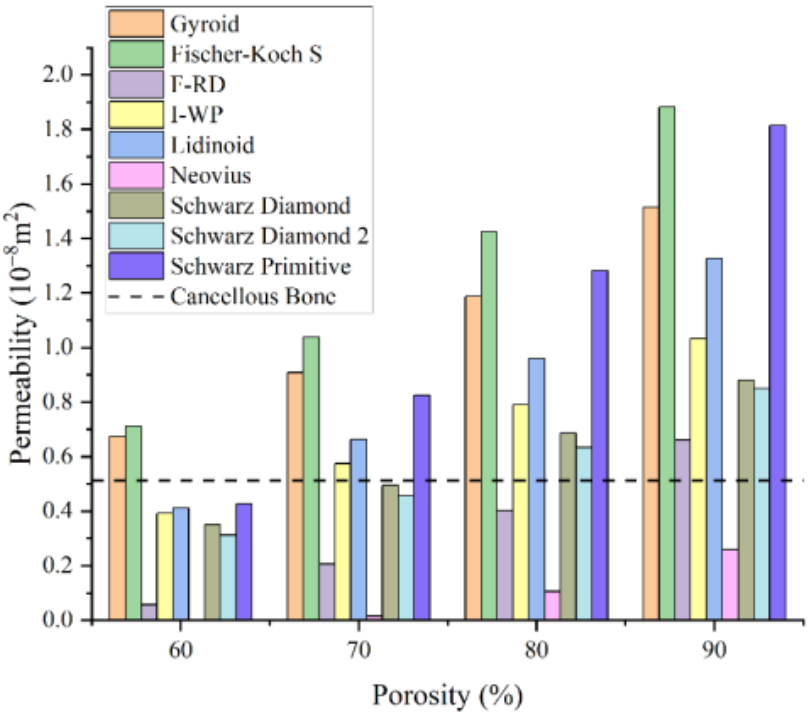

Fig. 19. Comparison diagram of permeability of scaffolds designed in non-Newtonian blood model with human Cancellous bone

According to the description provided, the scaffolds of Gyroid, Fischer-Koch S, Schwarz-diamond, and Schwarz-diamond 2 have smaller Skewness and coefficient of variation than other scaffolds. Therefore, the wall shear stress distribution in these four scaffolds is almost homogeneous, which can cause cell proliferation and differentiation to be almost uniform. Thus, their permeability and surface area should be checked to select the best optimal performance from these four scaffolds. Therefore, the Fischer-Koch S scaffold can offer better performance than other scaffolds in the four available porosities if maximum permeability is considered. However, if the closest permeability to the Cancellous bone is considered, the Schwarz-diamond 2 scaffold can perform more effectively than the other scaffolds in the two existing porosities. Also, if the maximum available surface area and the average wall shear stress are considered for cell adhesion and proliferation, the Schwarz-diamond scaffold at 80% porosity and the Schwarz-diamond 2 scaffold at 90% porosity will perform better than other scaffolds. As can be seen, selecting the most desirable scaffolds is a complex and challenging process and must be selected according to their conditions and applications. However, these four scaffolds performed best in their existing porosity among the nine designed scaffolds. It should be noted that this conclusion is valid only for normal bone needs.

5- Conclusion

This study aimed to investigate the characteristics affecting bone growth, such as permeability, wall shear stress, surface-to-volume ratio, and the selection of the most desirable scaffolds based on them. The results of this study can be summarized as follows:

- The numerical simulation results revealed that the permeability and the wall shear stress depend on the geometry and porosity of the scaffold. The permeability of the non-Newtonian model cannot be dimensionless due to viscosity variations, unlike the Newtonian model, i.e., in a fixed architecture. However, in different dimensions, the permeability of the non-Newtonian model will be different. It was also observed that the pressure drop in the non-Newtonian model is greater than in the Newtonian model under the same boundary conditions. Due to that, the permeability of the Newtonian model is higher than the non-Newtonian model.
- It was observed that with increasing porosity in some scaffolds, the path of scaffold pores changed from linear to nonlinear. In other words, the number of scaffold twists and bends increased, which increased the number of scaffold twists and bends surface of the scaffold. So this has led to nonlinear variations in permeability to scaffolds.
- Considering the permeability of Cancellous bones, scaffolds that effectively mimic the characteristics of this type

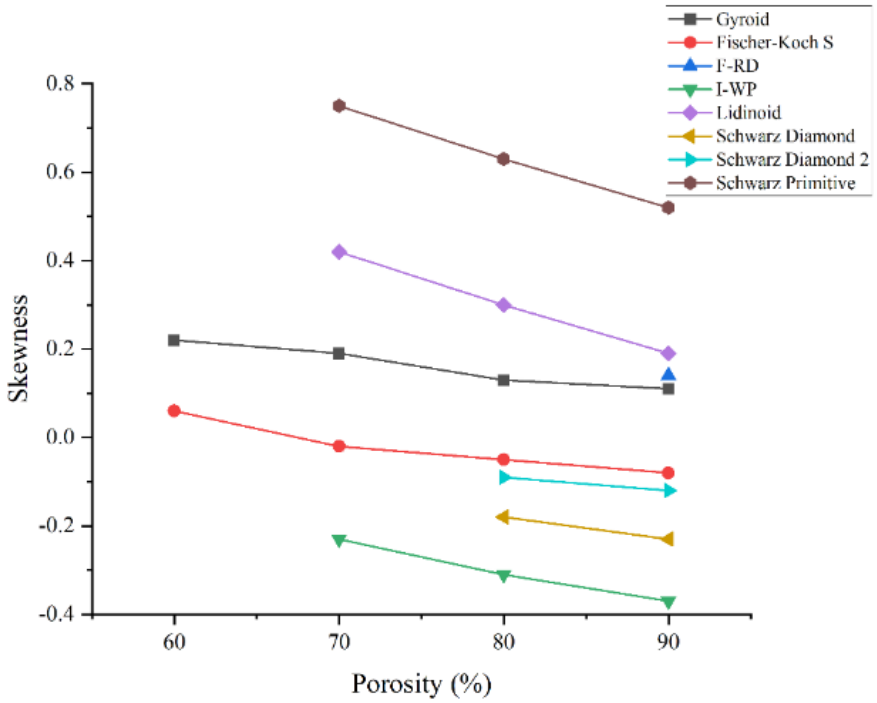

(a)

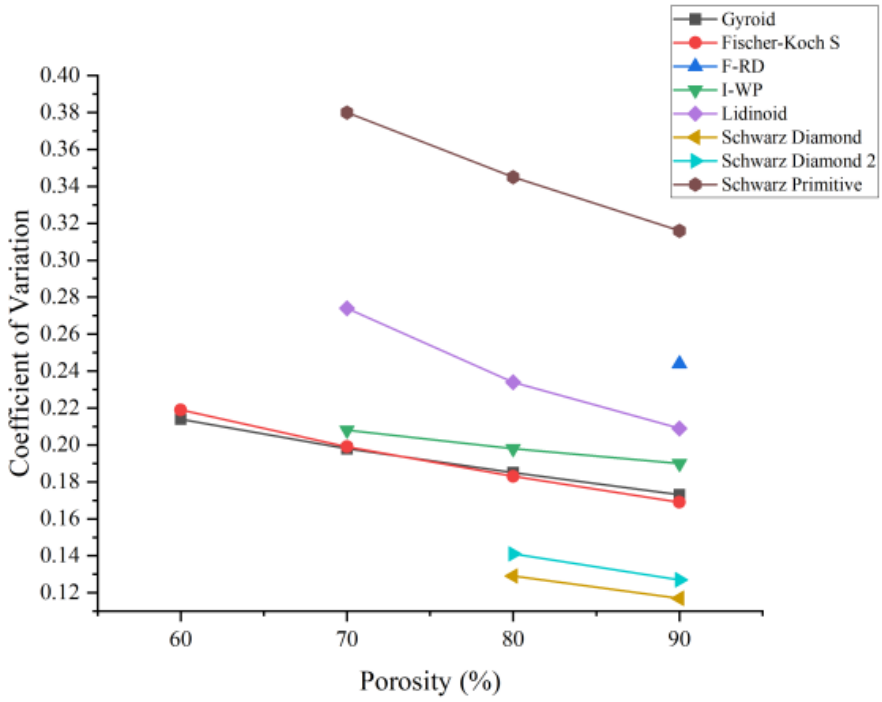

(b)

Fig. 20. Comparison diagram of a) Skewness and b) coefficient of variation of scaffolds in different porosities

of bone were identified. Then, using scaffolds' wall shear stress distribution, scaffolds with symmetrical and uniform wall shear stress were identified, which included Gyroid, Fischer-Koch S, Schwarz-diamond, and Schwarz-diamond 2 scaffolds.

- The wall shear stress varied with the channel inlet velocity, and in addition, it was observed that the distribution of the wall shear stress in scaffolds is very different. This makes the design of scaffolds based on the optimal distribution of the wall shear stress a difficult task in tissue engineering.
-

References

[1] Y. Lu, L. Cheng, Z. Yang, J. Li, H. Zhu, Relationship between the morphological, mechanical and permeability properties of porous bone scaffolds and the underlying microstructure, PLoS One, 15(9) (2020) e0238471-e0238471.

[2] L. Polo-Corrales, M. Latorre-Esteves, J. Ramirez-Vick, Scaffold Design for Bone Regeneration, Journal of nanoscience and nanotechnology, 14 (2014) 15-56.

[3] M.A. Velasco, C.A. Narváez-Tovar, D.A. Garzón-Alvarado, Design, Materials, and Mechanobiology of Biodegradable Scaffolds for Bone Tissue Engineering, BioMed Research International, 2015 (2015) 729076.

[4] F.S.L. Bobbert, K. Lietaert, A.A. Eftekhari, B. Pouran, S.M. Ahmadi, H. Weinans, A.A. Zadpoor, Additively manufactured metallic porous biomaterials based on minimal surfaces: A unique combination of topological, mechanical, and mass transport properties, Acta Biomaterialia, 53 (2017) 572-584.

[5] Z. Wang, C. Huang, J. Wang, P. Wang, S. Bi, C.A. Abbas, Design and Simulation of Flow Field for Bone Tissue Engineering Scaffold Based on Triply Periodic Minimal Surface, Chinese Journal of Mechanical Engineering, 32(1) (2019) 19.

[6] S. Ma, Q. Tang, Q. Feng, J. Song, X. Han, F. Guo, Mechanical behaviours and mass transport properties of bone-mimicking scaffolds consisted of gyroid structures manufactured using selective laser melting, Journal of the Mechanical Behavior of Biomedical Materials, 93 (2019) 158-169.

[7] A.P.G. Castro, T. Pires, J.E. Santos, B.P. Gouveia, P.R. Fernandes, Permeability versus Design in TPMS Scaffolds, Materials, 12(8) (2019) 1313.

[8] D. Ali, M. Ozalp, S.B.G. Blanquer, S. Onel, Permeability and fluid flow-induced wall shear stress in bone scaffolds with TPMS and lattice architectures: A CFD analysis, European Journal of Mechanics - B/Fluids, 79 (2020) 376-385.

[9] H. Chen, Q. Han, C. Wang, Y. Liu, B. Chen, J. Wang, Porous Scaffold Design for Additive Manufacturing in Orthopedics: A Review, Frontiers in Bioengineering and Biotechnology, 8 (2020).

[10] M.R. Dias, P.R. Fernandes, J.M. Guedes, S.J. Hollister, Permeability analysis of scaffolds for bone tissue engineering, Journal of Biomechanics, 45(6) (2012) 938-944.

[11] S. Ma, Q. Tang, X. Han, Q. Feng, J. Song, R. Setchi, Y. Liu, Y. Liu, A. Goulas, D.S. Engstrøm, Y.Y. Tse, N. Zhen, Manufacturability, Mechanical Properties, Mass-Transport Properties and Biocompatibility of Triply Periodic Minimal Surface (TPMS) Porous Scaffolds Fabricated by Selective Laser Melting, Materials & Design, 195 (2020) 109034.

[12] D. Ali, S. Sen, Finite element analysis of mechanical behavior, permeability and fluid induced wall shear stress of high porosity scaffolds with gyroid and lattice-based architectures, Journal of the Mechanical Behavior of Biomedical Materials, 75 (2017) 262-270.

[13] M. Zhianmanesh, M. Varmazyar, H. Montazerian, Fluid Permeability of Graded Porosity Scaffolds Architectured with Minimal Surfaces, ACS Biomaterials Science & Engineering, 5(3) (2019) 1228-1237.

[14] D. Ali, S. Sen, Permeability and fluid flow-induced wall shear stress of bone tissue scaffolds: Computational fluid dynamic analysis using Newtonian and non-Newtonian blood flow models, Computers in Biology and Medicine, 99 (2018) 201-208.

[15] X.-Y. Zhang, X.-C. Yan, G. Fang, M. Liu, Biomechanical influence of structural variation strategies on functionally graded scaffolds constructed with triply periodic minimal surface, Additive Manufacturing, 32 (2020) 101015.

[16] S.J.P. Callens, C.H. Arns, A. Kuliesh, A.A. Zadpoor, Decoupling Minimal Surface Metamaterial Properties Through Multi-Material Hyperbolic Tilings, Advanced Functional Materials, 31(30) (2021) 2101373.

[17] H.A. Zaharin, A.M. Abdul Rani, F.I. Azam, T.L. Ginta, N. Sallih, A. Ahmad, N.A. Yunus, T.Z.A. Zulkifli, Effect of Unit Cell Type and Pore Size on Porosity and Mechanical Behavior of Additively Manufactured Ti6Al4V Scaffolds, Materials, 11(12) (2018) 2402.

[18] B. Zhang, K. Mhapsekar, S. Anand, Design of Variable-Density Structures for Additive Manufacturing Using Gyroid Lattices, in: ASME 2017 International Design Engineering Technical Conferences and Computers and Information in Engineering Conference, 2017.

[19] J. Maszybrocka, B. Gapiński, M. Dworak, G. Skrabalak, A. Stwora, The manufacturability and compression properties of the Schwarz Diamond type Ti6Al4V cellular lattice fabricated by selective laser melting, The International Journal of Advanced Manufacturing Technology, 105(7) (2019) 3411-3425.

[20] N. Sreedhar, N. Thomas, O. Al-Ketan, R. Rowshan, H.H. Hernandez, R.K. Abu Al-Rub, H.A. Arafat, Mass transfer analysis of ultrafiltration using spacers based on triply periodic minimal surfaces: Effects of spacer design, directionality and voidage, Journal of Membrane Science, 561 (2018) 89-98.

[21] M.M. Sychov, L.A. Lebedev, S.V. Dyachenko, L.A. Nefedova, Mechanical properties of energy-absorbing structures with triply periodic minimal surface topology, Acta Astronautica, 150 (2018) 81-84.

[22] H.G. von Schnering, R. Nesper, Nodal surfaces of Fourier series: Fundamental invariants of structured matter, Zeitschrift für Physik B Condensed Matter, 83(3) (1991) 407-412.

[23] D. Ali, S. Sen, Computational Fluid Dynamics Study of the Effects of Surface Roughness on Permeability and Fluid Flow-Induced Wall Shear Stress in Scaffolds, Annals of Biomedical Engineering, 46(12) (2018) 2023-2035.

[24] W.C. Chin, Chapter 9 - Transient, Three-Dimensional, Multiphase Pipe and Annular Flow, in: W.C. Chin (Ed.) Managed Pressure Drilling, Gulf Professional Publishing, Boston, 2012, pp. 315-385.

HOW TO CITE THIS ARTICLE

A. Parandvash, M. Rezaei, E. Khavasi, Triply Periodic Minimal Surfaces Scaffolds and Their Comparison with Cancellous Bone: Fluid Flow Point of View, AUT J. Mech Eng., 6 (3) (2022) 443-466.

DOI: 10.22060/ajme.2022.20549.6005